Influence of beam diameter on Laser Powder Bed Fusion (L-PBF) process

M.C. Sow, T. De Terris, O. Castelnau, Z. Hamouche, F. Coste, R. Fabbro, P. Peyre

PIMM, Arts et Metiers Institute of technology, CNRS, CNAM, HESAM University, 151 Bd de l'Hopital, 75013 Paris, France

Keywords:
Conduction Welding mode
additive manufacturing
Volume Energy Density
Energy per Built Volume
L-PBF

A B S T R A C T

The use of large beams in the Laser Powder Bed Fusion (L-PBF) process has been receiving increasing attention for the past few years and may widen the dissemination of this technology in the industry, as well as help increase the production volume. In this paper, a detailed comparison is presented between a usual 80 µm diameter Gaussian laser spot and a 500 µm diameter top-hat laser beam. The following benefits of a large and homogeneous beam could be demonstrated: (1) a moderate increase of productivity by reducing the number of scan lines, (2) a nearly total suppression of spatters and powder bed degradation (local loss of powder homogeneity caused by the redeposition of spatters) due to the low volume energy densities carried out and the limitation of deleterious vaporization effects, (3) the manufacturing of near fully dense Inconel 625 parts, especially in the hatching zones. Last, the occurrence of larger thermal effects induced by the large beam L-PBF was discussed by comparing two distinct definitions of the laser energy density: at a local (melt pool) scale, and at a global (the whole manufactured part) level.

1. Introduction

The Laser Powder Bed Fusion (L-PBF) process is now considered to be the most powerful and efficient additive manufacturing process for building complex 3D shapes with a high degree of precision, combined with satisfactory metallurgical properties. Moreover, the building chambers have recently been enlarged, allowing the L-PBF manufacturing of up to 50-80 cm parts (SLM 800), with the simultaneous use of 4 lasers. Such characteristics are generally attractive for a range of industrial applications and materials, including the ones that are most reactive with oxygen (e.g. titanium, aluminum), or the ones that are most reflective to laser irradiations (e.g. copper).

However, several limitations still exist that prevent a wider dissemination of this process.

(1) First, physical phenomena like spatters or denudation occur during L-PBF. Matthews et al. [2] attributed such phenomena to vaporization phenomena and to the formation of a near-key-hole welding regime, due to intense power densities ($> MW/cm^2$). Khairallah et al. [3] explained more precisely that spatters and denudation are both assumed to be due to particle entrainment towards laser tracks, due to a lateral induced gas flow provoked by the shear between the upwards metal vapor plume and the Argon atmosphere. The resulting effect is a severe deterioration of powder beds by large spatters, which can disrupt powder spreading, generate porosities or defects and, above a certain defect size, stop the production. Qiu et al. [4] revealed that such metallic spatters either contaminate the powder bed surface or directly incorporate as inclusions on final parts.

(2) Even after process optimization, porosities are systematically present in L-PBF parts, with porosity rates depending on process parameters (laser Power P, laser spot diameter D, scan speed V) and minimum values achievable dependent on materials. Qiu et al. [4] and Ma et al. [5] working respectively on Ti6Al4V (with optical micrography + image analysis) and 304 L stainless steel (with Archimede's method) indicate less than 0.1 % porosity rate whereas Colopi et al. [1] obtained 2 % minimum porosity on pure copper, due to its low IR laser absorption (< 5 %).

(3) Another limitation is, for large parts necessitating long production times (several days), there is gradual contaminatation of building chambers by metallic vapors containing nanoparticles as indicated by Charpentier et al. [6]. Because of laser absorption or Rayleigh diffusion, this contamination can affect the laser energy deposit on the powder bed and degrade the global quality and densification of parts.

(4) Even with the use of multiple laser sources, the build rate of L-PBF systems is still low compared with other additive manufacturing techniques such as direct energy deposition (DED) or electron beam melting (EBM). Using the common formulation of build rate given by eq.1, i.e neglecting the powder spreading steps, a rough estimation of usual build rates gives values of around 40 cm^3 /h for L-PBF (with hd = 120 µm, Δh = 100 µm, V = 1 m/s), 140 cm^3/h for DED (with hd = 2.5 mm, Δh = 1 mm, V = 0.016 m/s) and around 70-100 cm^3/h for EBM. Productivity enhancement can therefore be achieved either by increasing scanning speed, layer height, or beam diameter [7].

$$p^* = V.\ hd.\ \Delta h \tag{1}$$

With p* [mm^3/s] = build rate, V [m/s] = scan speed, hd [m] = hatch distance, ⊗h [m] = layer height

Since the early days of L-PBF, industrial systems use 100/500 W single mode fiber lasers with less than 100 µm spot diameters and a near Gaussian beam distribution. The resulting power densities (I = P/S, with S = laser spot area) of such laser are high (I > 1 MW/cm^2), and favor deep melt-pool penetrations (usually 100 µm to 200 µm) with easy re-melting of at least 2 previous layers. Fabbro [21] has analytically confirmed this assumption, indicating a direct dependence of a normalized penetration depth (e/D) with volume energy density (considered as VED ≈ P/(V.D^2)) in keyhole welding mode. However, such L-PBF regimes also have limitations:

(1) the laser intensity are usually superior to the vaporization thresholds, especially in the center of laser beams. In other words, high laser intensities and Gaussian distribution favor boiling effects, destabilize melt-pools and generate spatters.
(2) With such high intensity regimes, increasing production rate by increasing scanning speed or layer height is not possible because of process instabilities (balling, humping) investigated for instance by Gunenthiram et al. [9]. Buchbinder [10] added that such instabilities at high intensity are more predominant for low thermal conductivity materials. Bidare et al. [11] indicates that improvement nevertheless is possible using higher ambient pressure.

In short, small spot configuration has two main limitations: the production rate is limited and vapor-induced instabilities with subsequent ejection of spatters are always present. In recent years, L-PBF combining large beam and high power have been envisaged for productivity enhancement. In 2010, Schleifenbaum et al. [12] showed that increasing the build rate up to 8 mm^3/s is possible by increasing the laser power (600 W) and beam diameter (1 mm). A multi-laser beam strategy, including a 0.38 mm diameter laser beam, was also tested by Heeling [13]. However, in the cited work, the large beam laser was only used simultaneously with the small one, as a pre-heating source allowing to reduce thermal gradients and residual stresses.

Montero-Sistiaga et al. [14,15] showed a 2.5 times productivity increase for 316 L stainless steel manufacturing with the use of a 1 kW-0.7 mm diameter compared to a classical L-PBF process. Recently, SLM Solutions^{Gmbh} incorporated a large beam laser (0.7 mm) combined with a smaller one (< 100 µm) into their industrial SLM 280 H L set-up. Such a configuration was tested successfully by Huber et al. [16] on a Ti-6Al-4 V alloy and authors did not evidence differences in thermal distorsions between the small beam and large beam configurations. One also have to mention the interesting work of Metelkova et al. [17] stating that a large beam defocusing (up to D = 260 µm) combined with high power (400 - 800 W) and low speeds (100-250 mm/s) could increase the theoretical productivity of L-PBF process up to 18 mm^3/s compared to less than 3 mm^3 /s usual values. Last, Makoana et al. [18] have compared the use of a 240 µm beam and a 80 µm diameter beam for single L-PBF tracks built with similar power densities (obtained with a factor 9 increase of power for the large spot). They concluded that melt-pool instabilities above 0.5 m/s for the large beam was a limiting factor to increase productivity.

A L-PBF procedure combining large laser beam and low laser intensities is also expected to limit vaporization and subsequent spatters ejection. Moreover, microstructures are expected to be somewhat modified, due to different thermal cycles. Both aspects have been little studied to date. In the current work, even if productivity enhancement is also addressed, the objective was mainly to explore a conduction heating regime L-PBF, with a suppression of vaporization effects. As a reminder, process parameters (P, V, D) are usually unified in a Volume Energy Density (VED) formulation (eq.2) which directly affects the dimension – especially the penetration depth - of L-PBF tracks according to Rubenchik et al. [19].

$$VED = \frac{4P}{\pi D^2 V} \quad (2)$$

With VED = Volume energy density (J/m^3), P = laser power (W), V = scan speed (m/s), D = spot diameter

The selection of an optimum laser source (beam power and diameter) to limit vaporization is expected to be possible by considering keyhole energy density thresholds during laser-matter interaction. Considering the pioneer work by Hann et al [8], King et al. [20] estimated such energy thresholds considering the evolution of melt-pool penetration depths versus a normalized enthalpy ratio (= $\Delta H/h_s$) between input laser energy ⊗H (eq.3) and the melt enthalpy h_s (eq.4). For $(\Delta H/h_s) > 10$, the surface is melted and when $(\Delta H/h_s) > 25$, a keyhole mode is obtained on single fusion lines. Fabbro [21] obtained analytically a very similar threshold of $(\Delta H/h_s) = 16 - 20$ for reaching a keyhole mode.

$$\Delta H = \frac{A.\ P}{\sqrt{\pi \alpha V r^3}} \quad (3)$$

With < [m^2/s] = thermal diffusivity = K/>C_p, A = absorptivity (≈ 0.4 according to Trapp, [21]), P [W] = laser power, K [W/m/K] = thermal conductivity, r is the spot size of the laser beam.

$$h_s = \rho C_p (T_m - T_0) \quad (4)$$

With h_s [J/kg] = enthalpy to reach the melting temperature, C_p [J/kg/K] = specific heat, T_m [K] = melting temperature, T_0 [K] = ambient temperature

Using thermo-physical data shown in Table 1, $(\Delta H/h_s)$ values were calculated for various usual L-PBF conditions (small beam) and large beam irradiation such as those considered in the current paper. For large beam irradiation (D = 0.5 mm), and for the following experimental: P = 800 W- V = 0.4 m/s and 1000 W –V = 0.5 m/s, the enthalpy ratio $\Delta H/h_s$ = 9.3 and 10.4, whereas for classical small beam iradiations (D = 0.08 mm), and using P = 200 W – V = 0.8 m/s and P = 250 W – V = 1 m/s, $\Delta H/h_s$ = 18.5 and 20.5. Such results indicate that the use of large beams (500 µm in diameter) in the 800-1000 W range allows reducing by a factor 2 this parameter, which becomes lower than the expected keyhole threshold.

The objectives of the current work can be defined as follows:

- Investigating the influence of a 0.5 mm diameter beam – low VED L-PBF procedure on the geometry and stability of single tracks, and comparing it to a classical small spot LPF process
- Manufacturing 3D parts using the two L-PBF configurations (*large beam–low VED* versus small *beam–high VED*), and analyzing the resulting density and microstructures
- Using dedicated diagnostics implemented in a L-PBF prototype to compare the novel *large beam–low VED* L-PBF with a *small beam-high VED* process in order to assess the influence of reduced vaporization effects
- Estimating the productivity enhancement for a L-PBF process carried out in near-conduction welding mode.

Table 1
Physical properties of Inconel 625 (considered at T_0 = 298 K), data from Special Metals Corporation [23], absorptivity value from Trapp et al. [22].

Parameters	Inconel 625
> [kg/m^3]	8200
C_p [J/kg/K]	420
K [W/m/K]	10
< [m^2/s]	$2.9.10^{-6}$
A	0.4
T_m (K)	1600
T_b (K)	3100

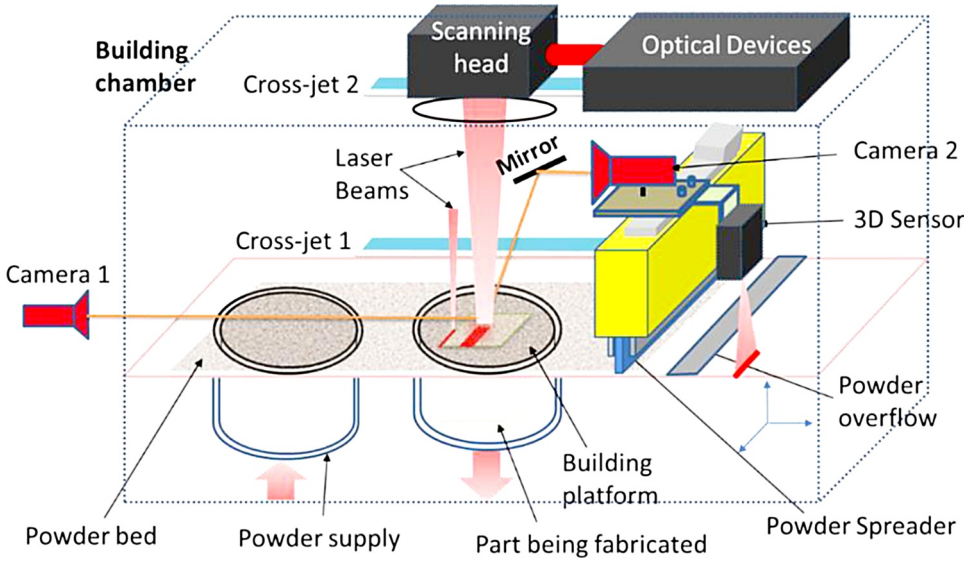

Fig. 1. Global scheme of the Instrumented L-PBF set-up (equipped with diagnostics).

2. Experimental procedure

2.1. L-PBF tests

Fig. 1 depicts the L-PBF prototype used in this work to test the capacity of a combined *small beam-high VED + large beam – low VED* irradiation, and to test various diagnostics (high-speed imaging, thermal measurements, 3D scanning, coaxial viewing, etc.) near the laser-powder bed interaction zone. A constant Argon flow (side cross-jet) was used to reach less than 1000 ppm O_2 rate in the building chamber before starting experiments.

The two laser sources used are:

(1) A 1 kW single-mode (redPOWER) / small laser spot (D = 80 µm) from SPI Lasers dedicated to the contours of the 3D part.
(2) A 2 kW multimode (YLR-2000-CT) / large and uniform laser spot (D = 500 µm) from IPG for the hatching zone, in order to limit vaporization and resulting instabilities, and to enhance productivity by reducing the number of fusion lines per built surface.

The shift from one laser to the other one is made possible via a selection mirror put on a motorized axis, positioned just before the scan head. Thanks to this device, the two lasers can work consecutively but not simultaneously.

The beam distributions, were analyzed with a Ophir-Optronics beam analyser equipped with a CCD camera (190 – 1100 nm), and positioned near the focus distance of a 420 mm lens (Fig. 2). A D = 80 µm Gaussian distribution is obtained for the single mode beam, and a 500 µm diameter top-hat distribution for the multimode source.

L-PBF tests were carried out using a gas-atomized Inconel 625 powder supplied by Praxair with particle diameters in the 15 µm - 45 µm range and a 22 µm mean diameter. For manufacturing 3D parts, powder was spread on a 150 mm diameter stainless steel building support using a polymer spreader system (= powder delivery system), resulting in approximately 50 % powder bed compactness. For the single line tracks, powder was manually deposited on 3 mm thick Inconel 625 plates. Both samples was sandblasted before powder deposition.

The following diagnostics have been implemented in the L-PBF set-up:

(1) Two Photron MC2 high speed (up to 10000 fr/s with reduced field) cameras for video recording of the fusion zone corresponding to a 10 mm x 10 mm window and a C-Mos sensor of 512 × 512 pixels resulting in a 10 µm/pixel resolution, and mounted with a low-band pass filter allowing to cut the 1.070 µm laser wavelength
(2) A LMI Go-Cator 3D sensor (*Stemmer Imaging*) using a 10 mm width laser line scanning of the powder bed, resulting in a 1 µm vertical and lateral resolution. The system allowed controlling the powder bed thickness and investigating the morphology of as-built surfaces.

The last two diagnostics were clamped directly on a (O,y) motorized axis (ACT Motion controller) mounted on the spreader system (Fig. 1), which allowed scanning the building platform before and after lasing and analyze different building areas with high speed cameras.

A range of L-PBF conditions has been tested and is summarized in Table 2, starting with single tracks, to select adequate parameters before building 3D parts. The main difference between *small beam-high VED* and *large beam – low VED* L-PBF is the 5 to 10 times lower volume energy density (VED) carried out with the *large beam – low VED*, which is expected to avoid vaporization effects.

2.2. Post mortem analysis of L-PBF samples

First, the surface finish of built surfaces was investigated using a Dektak Stylus 150 Veeco mechanical profilometer.

Single L-PBF tracks and 3D samples were then analyzed on cross-sections using a Zeiss Axio Imager optical microscope, after polishing up to 1 µm diamond suspension. The analysis of porosity rate was made using a x 50 magnification, resulting in a 1.37 µm/pixel resolution. Five images, corresponding to a 47.5 mm^2 analyzed area were captured and binarized using imageJ® software. The porosity rate was then estimated using the ratio of black pixels.

In a second step, microstructure was analysed on chemically etched samples by mean of a Philips XL40 scanning electron microscope equipped with an electron backscatter diffraction (EBSD) system, before and after a solution treatment at 1100 °C for 3 hours.

Last, a number of Hardness tests were carried out on a Clemex CMT HD microscope, with a 200 g load, to compare the local mechanical properties of L-PBF materials with or without heat treatment.

3. Results

3.1. Analysis of single L-PBF tracks

For parametric optimization, a series of single line scans were first

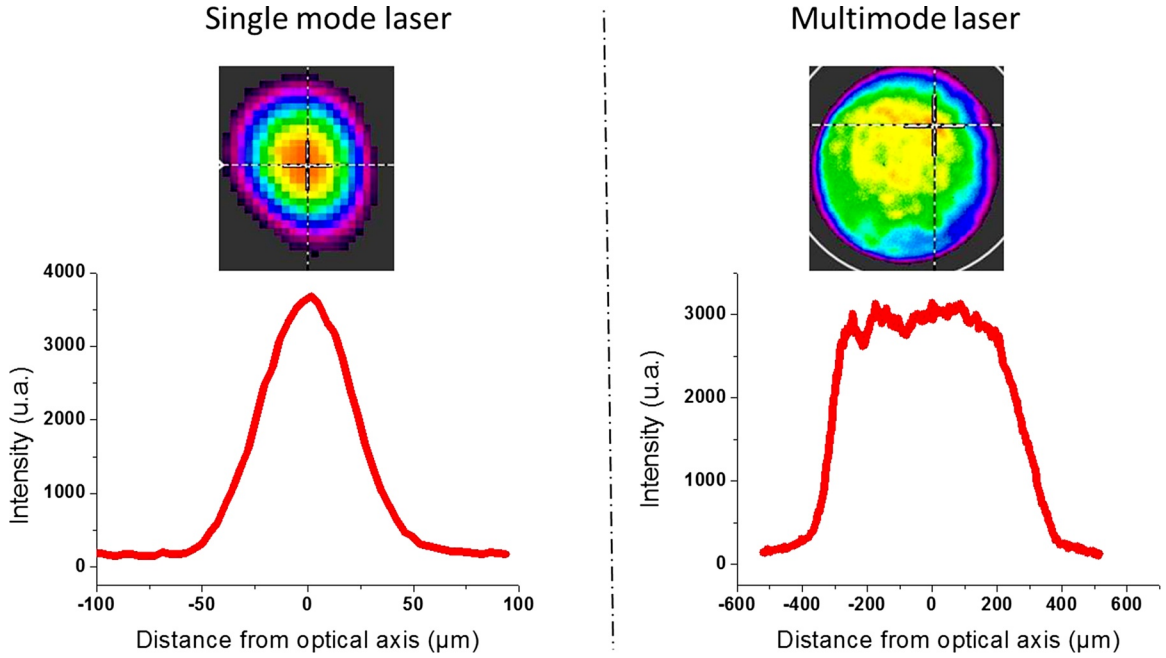

Fig. 2. Laser beam distributions for (a) the small laser spot, (b) the large multimode laser spot. Laser diameters at the focus point were considered at $1/e^2$ (D = 80 µm and 500 µm).

Table 2
Process parameters carried out on single tracks with small (D = 0.8 mm) or large (D = 0.5 mm) laser spots.

Parameters	Large spot	Small spot
P (W)	400 – 2000	200 – 800
Spot size D (mm)	0.5	0.08
V (m/s)	0.1 – 0.8	0.6 – 1.8
Hatch (µm)	200 – 500	70 – 120
Layer Height ⊗h (µm)	50	50
VED (J/mm^3)	5 – 101	20 – 200
% O_2	< 1000 ppm	< 1000 ppm

carried out on a 50 µm-thick powder layer (cf. Table 4). Similar VED windows (from 10 to 120 J/mm^3) were tested for both *small beam-high VED* and *large beam – low VED*; however, for the latter, we will mostly focus on small VED (≤ 25 J/mm^3). All data are presented in tables 3 and 4. The laser power and scanning speed were varied in order to explore a variety of parametric combinations (high power + low scanning speed, high power + high speed, low power + low scanning speed, mean power + low scanning speed, etc). Fig. 3 summarizes various cross-section morphologies obtained for *small beam-high VED* and *large beam – low VED*, whereas track depth versus VED are shown in Fig. 4 for both regimes. Based on these figures, several instructive results can be highlighted :

(1) As expected, *large beam–low VED* generates broader and flatter melt pool, whereas classical hemispherical shapes are obtained with *small beam-high VED*.
(2) Nail head track shapes are shown for *large beam–low VED* at higher VED (> 25 J/mm^3), assumed to be due to the key-hole welding mode. When decreasing VED, the morphologies become near elliptical and reflects a conduction welding mode.
(3) As expected from the analytical models of Fabbro [21] and Rubenchik [19], a linear increase of penetration depth was observed with VED (Fig. 4), for both *small beam-high VED* and *large beam–low VED*. This confirms the ability of VED to be used as a predictive estimation of the penetration depths.
(4) A similar remelted depth of 100 µm (usually considered as a minimum value for densification in L-PBF), can be obtained for lower (5 times lower) VED for the *large beam–low VED* configuration (VED ≈ 10 J/mm^3) compared to the *small beam-high VED* (VED ≈ 55 J/mm^3) configuration. This instructive result confirms that the use of *large beam–low VED* is well adapted for generating large-enough fusion depths in conductive welding mode, i.e without reaching a near-keyhole welding mode (Fig. 4). The lower 3D thermal (or more planar) dissipation for the large diameter is believed to be the main reason explaining the larger penetration depths. This statement is confirmed by analytical models of welding

Table 3
Analysis of single tracks obtained with the small beam configuration (D = 80 µm) (in italics, single tracks with balling).

spot size	P (W)	V (mm/s)	VED (J/mm3)	Depth (µm)	Width (µm)
80	200	400	99,5	171 +/-20	167 +/-22
80	200	600	66,3	105 +/-11	137 +/-15
80	200	700	56,8	84 +/-10	129 +/-18
80	200	800	49,7	69 +/-11	125 +/-19
80	200	1000	39,8	55 +/-10	111 +/- 15
80	200	1200	33,1	44 +/- 11	95 +/- 15
80	*200*	*1400*	*28,4*	*41* +/-12	*94* +/-18
80	*200*	*1600*	*24,8*	*34* +/-10	*87* +/-15
80	400	400	199,0	404 +/-32	202 +/-25
80	400	600	132,6	278 +/-30	188 +/-22
80	400	800	99,5	191 +/-15	173 +/-12
80	400	1000	79,6	147 +/-15	142 +/-20
80	400	1200	66,3	124 +/-17	116 +/-15
80	400	1400	56,8	104 +/-10	109 +/-12
80	400	1600	49,7	88 +/-12	112 +/-15
80	*400*	*1800*	*44,2*	*78* +/-10	*102* +/-19
80	400	2000	39,8	70 +/-15	96 +/-13
80	800	500	318,4	759 +/-46	201 +/-22
80	800	600	265,3	656 +/-28	210 +/-18
80	800	700	227,4	531 +/-33	216 +/-20
80	800	800	199,0	487 +/- 40	213 +/-25
80	800	1000	159,2	261 +/-23	170 +/-15
80	800	1200	132,6	290 +/-24	175 +/-19
80	800	1400	113,7	241 +/-20	165 +/-15
80	800	1600	99,5	214 +/-15	175 +/-18
80	800	1800	88,4	184 +/-12	160 +/-15
80	800	2000	79,6	162 +/-19	148 +/-17

Table 4
Analysis of single tracks obtained with the large beam configuration (D = 500 µm).

Spot size (µm)	P (W)	V (mm/s)	VED (J/mm^3)	Depth (µm)	Width (µm)
500	1000	25	203,7	1211 +/-71	1582 +/-78
500	1000	35	145,5	977 +/- 85	1399 +/- 70
500	1000	50	101,8	706 +/-50	1155 +/-79
500	1000	75	67,9	507 +/-35	1066 +/-64
500	1000	100	50,9	394 +/-37	993 +/-48
500	1000	150	33,9	254 +/-18	979 +/-32
500	1000	200	25,4	195 +/-18	898 +/-51
500	1000	250	20,3	163 +/-21	853 +/-35
500	1000	350	14,5	120 +/-12	839 +/-25
500	1000	500	10,1	78 +/-17	792 +/-29

indicating a linear dependence between (fusion depth / beam diameter) and VED as shown by Rubenchik et al. [19] and more recently Fabbro et al. [21]. For instance, for a similar low VED of around 20 J/mm^3, for which both conditions are assumed to generate a conduction welding mode, the penetration is 4 times deeper with the larger beam.

(5) A limited number of tracks carried out with the small diameter L-PBF have shown balling effects (for instance, tracks carried out with P = 200 W, V = 1.4 m/s and 1.6 m/s or with P = 400 W, V = 1.8 m/s : see Table 3). For the large beam L-PBF no-balling issues were shown.

Surface aspects of L-PBF tracks and surrounding powder bed were also investigated for a *large beam – low VED* configuration (Fig. 5) by 3D scanning. These profiles indicate:

- An increase of spatters re-deposited on powder bed and drastic decrease of tracks widths above 600 mm/s, attributed to unsufficient melt-pool dilution at high scanning speed (Fig. 5).
- Denudated zones (in blue) on both sides of tracks with a quite constant width of about 500-600 µm, whatever the VED values.
- A large oversize effect (+50/60 µm in height) at the beginning of each fusion line (in red-orange on Fig. 5). Such an effect, common on laser weld tracks, is due to the interaction between the liquid metal ejected backwards and the solidification front, when the melt-pool has not reached a permanent regime yet. This phenomenon is more severe than with *small beam–high VED* (+20 µm).

An interesting difference concerns denudation zones. Contrary to a classical high VED L-PBF process where, as explained by Matthews et al. [2], powder particles are entrained towards the melt-pool by a lateral induced gas flow provoked by the vapor plume, a different phenomenon is shown with the use of *large beam – low VED*. Here, the width of the denudation zone mostly corresponds to the width of the melt-pool in the substrate, and is associated with the formation of macro liquid droplets (100-250 µm) nearby the fusion track (Fig. 6), remelted by subsequent fusion tracks. This phenomenon is not fully understood yet and is still being investigated.

In conclusion, based on these previous results on single tracks, it

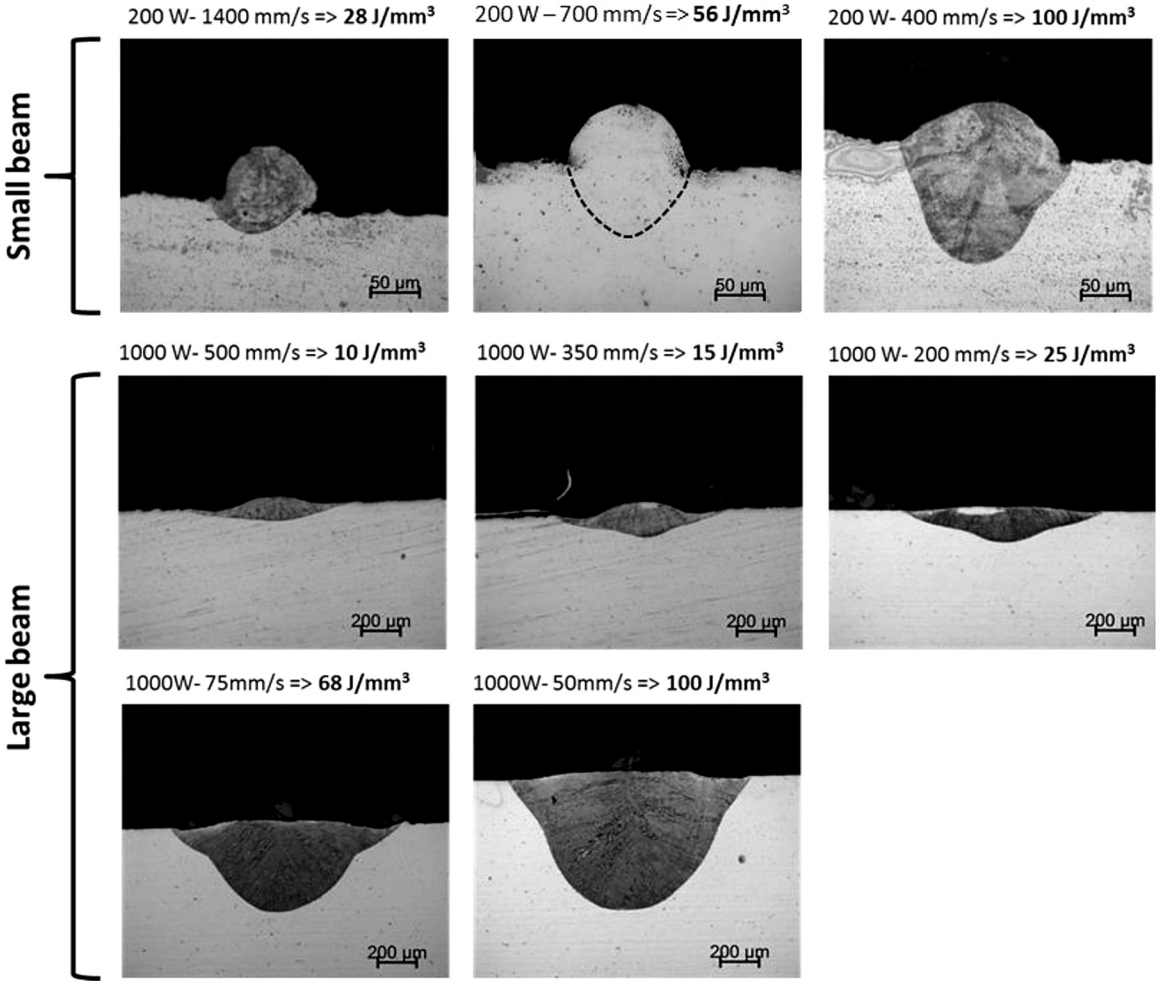

Fig. 3. Cross sections of L-PBF tracks obtained with small (D = 80 µm) and large (D = 500 µm) spots - Irradiation of 50 µm-thick powder layer deposited on a 2 mm-thick stainless steel substrate.

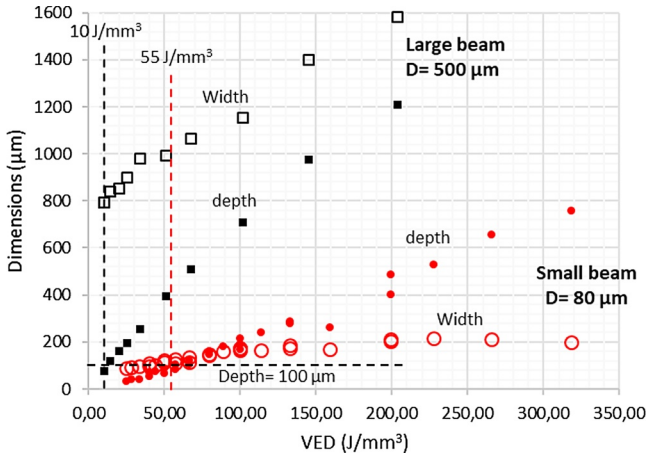

Fig. 4. Penetration depths and tracks widths (considered in the substrate) obtained for track on plate fusions versus VED for 2 laser configurations (small and large beams). A similar ~ 100 µm fusion depth can be obtained at much lower VED (10 J/mm^3 versus 55 J/mm^3) for large beams.

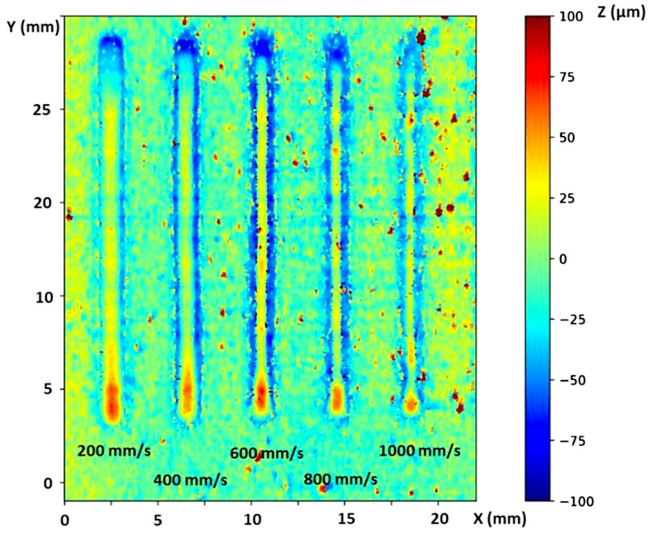

Fig. 5. 3D scanner of large beam (D = 500 µm) single tracks for P = 1000 W for various scan speeds. Denudated zones are in blue. Track discontinuities and spatters are visible at high scan speed. An oversize effect (in red-orange) is evidenced at the beginning of each fusion line, more pronounced for low scan speed.

was shown to be possible to obtain more than 100 µm fusion depths with the use of large beam and much lower VED (< 20 J/mm^3) than with the usual L-PBF procedure with *small beam-high VED* (VED > 50 J/mm^3). Such conditions (Table 5) generate elliptical and shallow melt pools, attributed to a conduction welding mode. The resulting effect of suppressing vaporization is also a reduction of spatters ejected during the process. However, a possible limitation is the formation of liquid droplets nearby the fusion zones, and an oversize effect at the beginning of each fusion track.

3.2. Manufacturing and analysis of 3D parts

3.2.1. L-PBF conditions

Based upon optimal process parameters identified on single tracks (Table 2), a range of *Large beam – Low VED* process conditions (Table 3) have been mostly compared to a usual *small beam-high VED* condition in terms of surface morphology, density and process stability, as well as microstructures formed. For all conditions (small and large beams), carried out on 15 × 15 mm cubes, a rotation angle in between layers was fixed to 67°. Moreover, for a sake of clarity, samples have been built without contours, i.e only in hatching mode.

Another definition of volume energy termed energy per built volume EBV was also reported in Table 5 to define the amount of energy really absorbed per built volume in a 3D part. Compared with the VED formulation (eq. 2) which allows estimating the penetration depth generated by laser matter interaction during a single track and traduces an instantaneous volume energy deposit, the analytical formulation of EBV (eq.5) reflects the total energy provided into a 3D built volume. Such a formulation has been used already by Gu et al. [24] on 316 L and Criales et al. [25] on Inconel 625. In the current work, due to the large beam diameter range (0.08 mm versus 0.5 mm), the comparison of VED and EBV formulation makes particular sense.

$$EBV = \frac{A\,P}{hd\,\Delta h\,V} \tag{5}$$

With EBV = deposited Energy per Built Volume (J/m^3), A = laser absorptivity, P = incident laser power (W), hd hatch distance (m), ⊗h = layer height (m), V = scan speed (m/s)

Considering such a EBV formulation, it appears that +20 % to +220 % higher energy inputs per built volume are used with the *large beam – low VED* configuration (Table 5) during the manufacturing of a 3D part with a similar layer height ⊗h, whereas VED values are 2 to 5 times lower. For that estimation, we have considered that the laser absorptivity for *Large beam-Low VED* is about 0.4 (characteristic of conduction mode on Inconel 625) and increases up to 0.8 for *small beam-high VED* configuration (characteristic of keyhole regime), as indicated by Trapp et al. [22] on 316 L.

3.2.2. Results

The *small beam-high VED L-PBF* configuration carried out is rather typical of usual L-PBF conditions and builds samples with a rather large roughness (Fig. 7) on top of the building surface (Sa = 20 +/- 5 µm), a satisfactory dimensional match compared with CAD data (around 0.15 mm difference for cubic samples with a 15 mm edge), and a porosity density (estimated on metallurgical cross-sections) comprised between 0.3 and 0.5 % surface ratio, depending on process conditions. However, it has to be mentioned here that a real process optimization (without just considering recommended parameters) would have certainly allowed reducing this porosity rate.

Large beam – Low VED samples globally exhibit much smoother and stable building surfaces (Sa = 3-5 µm), but a tiny curvature (gap = 100 µm) between the center and the edges of the squared sample (Fig. 7) is inherited from oversize effects (Fig. 5).

High speed videos captured on both configurations reveal a much more stable process with the *large beam – low VED* irradiation, with considerably less spatters ejected. This behaviour is typical of a stable conduction welding mode (Fig. 8) with a limited vaporization.

A preliminary analysis of samples on metallurgical cross-sections indicates that they are almost fully dense for *large beam – low VED* (no porosity detected using optical microscopy), whereas porosities are always present in classical L-PBF samples (Fig. 9), with a 0.3-0.5 % surface ratio. This is a particularly interesting point which confirms that the physical origin of porosities is mostly vaporization and keyhole, large depth/width ratios favoring melt-pool instabilities.

A + 20 to +50 % increase of build rate p* is evidenced for the large beam – low VED configuration (Table 5). Such an increase is lower than expected because of the rather short hatch distance optimized with large beams (hd ~ 0.5 D), compared with what is usually obtained with small beam diameters (hd ~ 1 to 1.2 D). The main reason for that is that built tracks (with added matter) are thinner than fused tracks when using a large laser beam (Fig. 3), which requires a shorter hatch spacing to ensure a similar overlap between built areas.

The limitation of hatch spacing for *large beam – Low VED* process is illustrated in Fig. 10.

Finally, it is worth noting an undesired effect of the *Large beam – low*

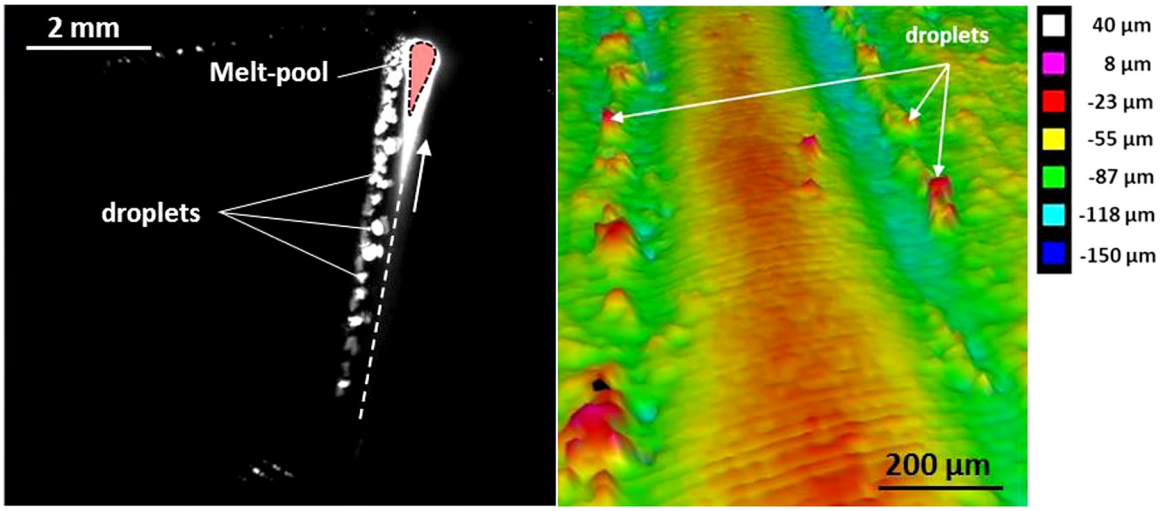

Fig. 6. Formation of liquid droplets (without spatters) near the fusion lines during the large beam – low VED L-PBF process (a) high speed image, (b) 3D scan of a L-PBF track.

Table 5
Comparison of VED and EBV values for large and small spot configuration (⊗h = 50 µm), p* was calculated considering eq.1 (laser absorptivity A = 0.4 and A = 0.8 have been used for the calculation of EBV with large and small spot diameters respectively).

	P (W)	D (µm)	V (m/s)	Hatch hd (µm)	VED (J/mm^3)	EBV (J/mm^3)	p* (mm^3/s)	Porosity rate (%)
Small spot	200	80	0.8	120	50	33	4.8	0.5
Large spot -1	800	500	0.2	300	20	106	3	0
	800	500	0.4	200	10	80	4	0
	800	500	0.6	200	7	40	6	0.02
Large spot -2	1000	500	0.4	250	13	80	5	0
	1000	500	0.8	200	6	50	8	0.05

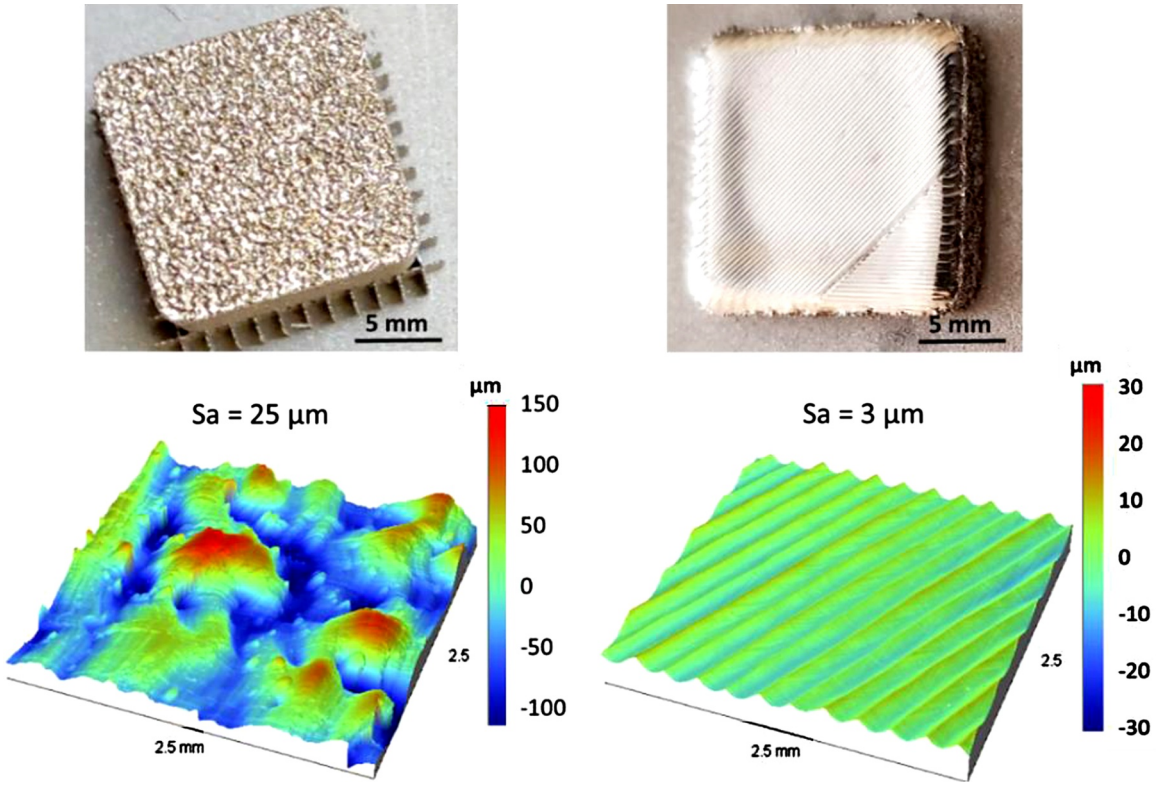

Fig. 7. Examples of 15 mm x 15 mm squared L-PBF samples - (a) 80 µm spot (200 W – 0.8 m/s – hatch = 120 µm, VED = 32 J/mm^3), (b) 500 µm spot (800 W, 0.4 m/s, hatch = 200 µm, VED = 10 J/mm^3): a smoother build surface is obtained with the large beam – low VED.

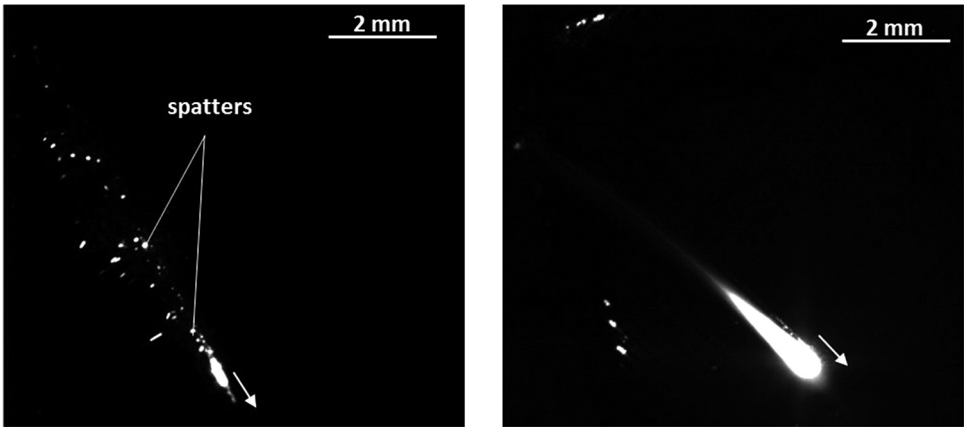

Fig. 8. High-speed imaging of L-PBF tests using (left image) a 80 µm laser spot (P = 200 W, V = 0.8 m/s), (right image) a 500 µm laser spot (P = 800 W, V = 0.4 m/s): less spatters are generated with large spots -low VED.

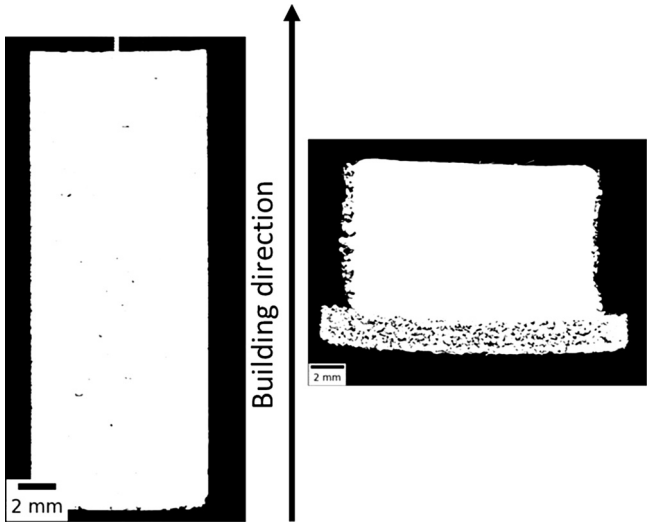

Fig. 9. comparison of small beam (left) and large beam – low VED irradiation (right) beam cross-sections in terms of porosity rates. Large beam – low VED exhibits fully dense material but promotes thermal deformations.

VED at a macroscopic scale, in terms of thermally-induced deformations (Fig. 9) that tend to generate a bending curvature of the samples. Such deformations are attributed to the high total energy input (EBV). Preliminary temperature measurements versus time tend to confirm this assumption and indicate that higher (+200 °C) average temperature in L-PBF parts for *large beam – low VED* samples than for *small beam – high VED* conditions. "In the same context, the samples made without contours showed a high lateral surface roughness for large beam – low VED parts. This can also be explained by the high temperature rise which led to the agglomeration of powder in the vicinity of the part being manufactured."

For future applications, thermal distorsions could be limited by a preheating of the building platform.

3.3. Microstructural investigation

In a second step, samples were etched to reveal microstructures (Fig. 11) using a 92 % HCl /5 % H_2SO_4/ 3% HNO_3 reagent. It was confirmed that *large beam – low VED* provide broader and nearly planar melt-pools with relatively low penetration depths (~150 µm) for the investigated conditions. Comparatively, nearly similar penetration depths (~130 µm) are obtained with a *small beam-high VED*, but with 4 times thinner melt-pools (150 µm versus 600 µm), resulting in more hemispherical melt-pool shapes (Fig. 11b). This confirms that *large beam – low VED* condition promoted a conduction welding regime with a depth-over-beam diameter ratio of 0.3 (= 150/500) whereas *small beam-high VED* condition generated a keyhole regime with a depth-over-beam diameter ratio of 130/73 = 1.7.

At higher magnification, optical microscopy reveals a microstructure composed of cells growing perpendicular and parallel to the building direction for both L-PBF conditions. The analysis of inter-cell distance (ICD) indicates average values of 2.3 µm for D = 0.5 mm/ VED = 13 J/mm^3 versus 0.9 µm for D = 0.08 mm / VED = 50 J/mm^3, which traduces lower cooling rates (K/s) for D = 0.5 mm. An estimation of corresponding cooling rates was carried out with the use of eq.6 proposed by Stefanescu [26]. Values of 4.10^5 K/s for D = 0.08 mm / 50 J/mm^3 and 10^4 K/s for D = 0.5 mm / VED = 13 J/mm^3 were obtained.

Despite this microstructural difference, similar hardness values ($HV_{0.2}$ = 310 +/- 15) were shown on both as-built samples.

$$ICD = w.\ Q^{-c} \quad (6)$$

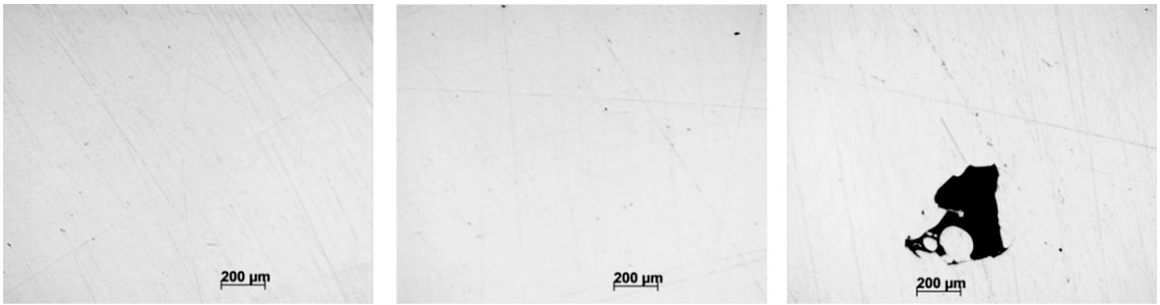

Fig. 10. Cross-sections of L-PBF samples using a D = 500 µm laser spot for different hatch distances hd (P = 800 W, V = 400 mm/s): (left) hd = 200 µm, (middle) H = 300 µm, (right) hd = 400 µm.

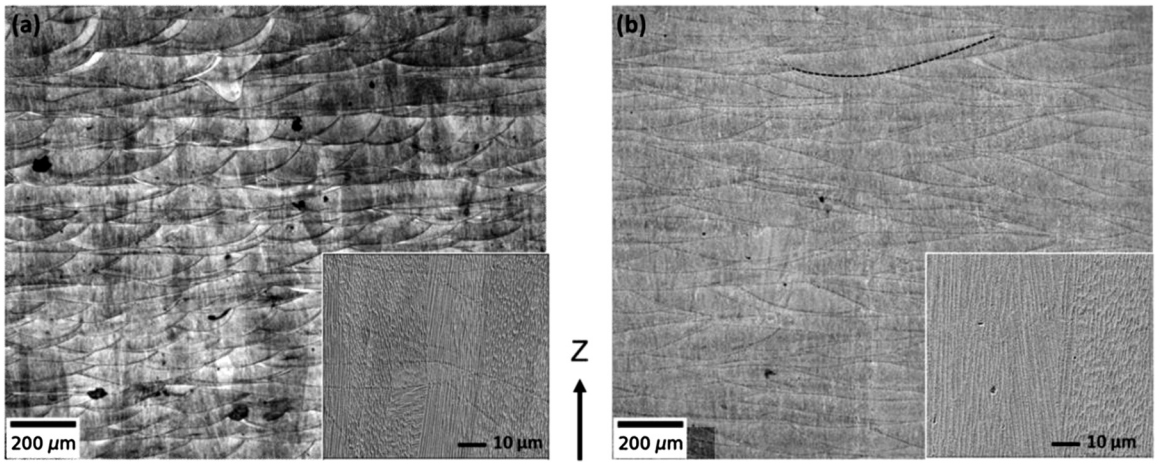

Fig. 11. Scanning electron microscopy showing melt pool morphologies of both small beam-high VED (a) and large beam – low VED (b) conditions. Inserted images revels very similar cells growing perpendicular and parallel to the building direction (Z), P = 200 W – V = 0.8 m/s for D = 0.08 mm and P = 1000 W, V = 0.4 m/s for D = 0.5 mm.

With ICD = Inter-cell distance, w,c = material dependent constants (w = 50 µm and c = -0.33 on Ni-based alloys,), Q = cooling rate ($K.s^{-1}$)

A detailed EBSD analysis of columnar grain structure for both L-PBF conditions is shown in Fig. 12. Grains are always oriented along the build direction but appear longer (sometimes more than 1 mm in height) and larger for the *large beam- low VED* condition. In order to show the maximum length of the large beam grain, the magnification of the two images have been adjusted. This result tends to confirm a hotter *large beam- low VED* regime associated with lower cooling rates. Future works should investigate further this aspect, for instance by making more or less simplified FE simulation of the laser fusion, and taking into account an average temperature of irradiated parts dependent on the main L-PBF parameters.

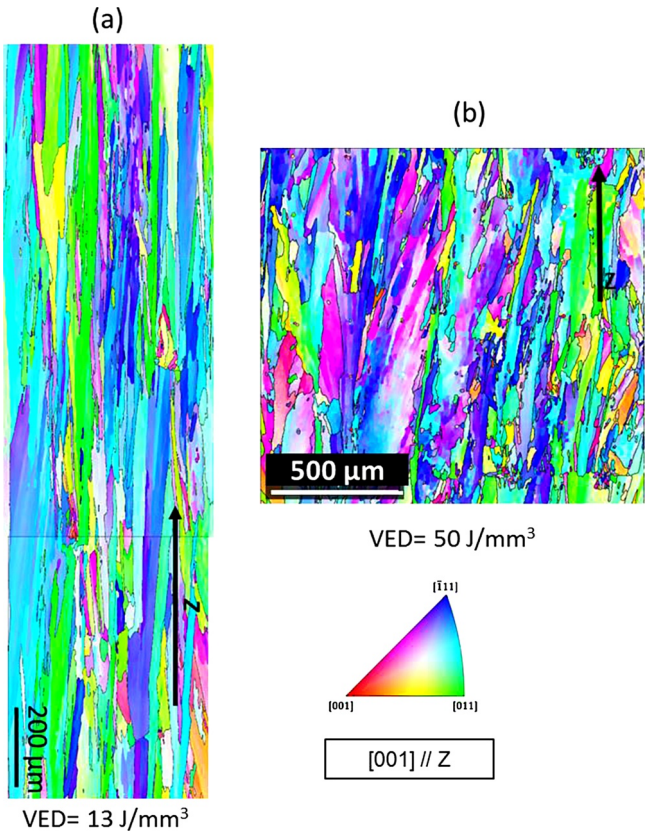

Fig. 12. EBSD images for samples built with large beam-low VED (a) and small beam-high VED (b). The analysis of intra-grain mosaicity/misorientation was used to estimate dislocation density.

In a second step, EBSD analysis was used to analyze intra-grains structure by estimating the amount of geometric necessary dislocations (GND) for both *small beam-high VED* and *large beam – low VED* configuration. This can revealed inside grains by the analysis of local mosaicity. As indicated by Gao [27], GND density reflects the local misorientation inside grains. This value can be obtained through the Kernel average misorientation (KAM) from EBSD maps which translates the amount of stored energy, with the use of eq. 7 proposed by Moussa [28].

$$\rho_{GND} = \frac{\alpha \times \theta}{b \times x} \tag{7}$$

With ρ_{GND} = density of geometrically necessary dislocations (en m. m^{-3}), α a constant comprised between 2 and 4, θ = KAM (in °), b = Burgers vector (m), x = EBSD map acquisition step (m)

A Matlab-Mtex toolbox combined with an in house development of dedicated scripts was used for mapping and averaging the GND distribution through the analysis of intra-grain mosaicity. Similar average ρ_{GND} values were obtained for the two L-PBF conditions : 2.2 10^{15} m. m^{-3} for 0.08 mm – 50 J/mm^3 condition and 1.9 10^{15} m. m^{-3} for 0.5 mm – 13 J/mm^3. Such values are incredibly high compared with conventional cast processing, and are close from dislocation densities of severely work-hardened materials. They probably result from high deformation rates during melt-pool shrinkage, and are usually located near the inter-cell boundaries as shown with transmission electron microscopy by Salman [29] on 316 L stainless steel. In this case, the change of cooling rate associated with the change of L-PBF regime was not sufficient to modify the dislocation density.

The corresponding stored elastic energy is known to allow L-PBF materials to recrystallize during subsequent heat treatment at high temperature, like severely work-hardened metals.

This phenomenon was analyzed on both L-PBF conditions with a solid solution heat treatment (1100 °C – 3 h) classical for Inconel 625 alloy according to Kreitcberg [30]. After heat-treatment, the morphological and crystallographic oriented texture along the building direction was deleted and turned into fully recrystallized equiaxed microstructures for both L-PBF conditions. The resulting average grain size after heat-treatment was about 30-50 µm for the *small beam-high VED* (Fig. 13b), and 50-100 µm for the *large beam-low VED* (Fig. 13a).

The heat-treatment also decreased the hardness (230 $HV_{0.2}$) and reduced the dislocation density ρ_{GND} to 5-7. 10^{13} m. m^{-3} values (40 times lower than on as–built samples).

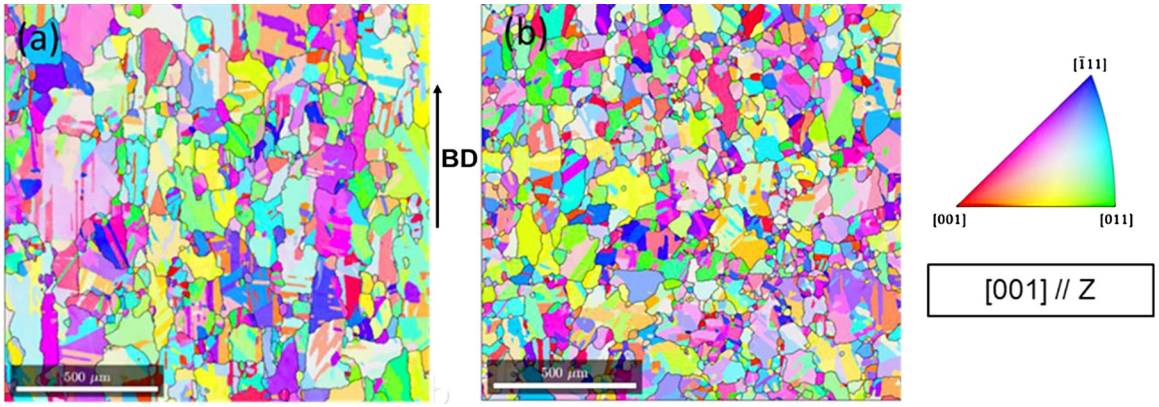

Fig. 13. EBSD images after solution treatment for samples built with large beam-low VED (a) and small beam-high VED (b).

It has to be pointed out that the hardness levels obtained on both as-built and solutionized L-PBF samples are assumed to be more dependent on the dislocation density that on the grain-size or inter-cell distances (Hall-Petch effect).

3.4. Combination of small beam-high VED and large beam – low VED configurations

Various tests have been carried-out combining small spot (0.08 mm) irradiation for the contour parts and *large beam – low VED* (0.5 mm – 12 J/mm^3) for hatching areas in order to validate a combined single mode / multimode laser procedure for manufacturing 3D parts.

Results (Fig. 14) mostly confirm the interest of combining *large beam – low VED* and *small beam – high VED* irradiations: the contour is geometrically well defined due to the small spot (80 µm) whereas the inner part is fully dense due to the *large beam – low VED* irradiation. A complex issue to overcome was the optimization of the offset distance zone between contour and hatching, which is dependent on process conditions: the larger the scan speed (0.4 to 0.8 m/s), the lower the offset distance (170 µm to 100 µm). This was mostly due to larger denudation zones near the turn point during hatching with a *large beam – low VED*. For this reason, a (contour → hatching) procedure combined with an optimized offset distance was more satisfactory than a (hatching → contour) mode in stabilizing the contour-hatching transition. The main effect was a reduction of oversize effects (Fig.5) at the beginning of hatching vectors (= external border of hatching area) due to a reduced powder feeding of the melt-pool. Moreover, due to large EBV in the hatching zone resulting in higher wall temperatures, more particle agglomerations are shown, which tend to promote larger side roughness. This will have to be considered more in detail in future works, even if the use of contours has significantly improved the surface finish.

4. Conclusion

The use of *large beam – low VED* was experimentally shown to provide significant improvements to the powder bed L-PBF process in terms of process stability, reduction of spatters and density of manufactured parts. The reduction of vaporization effects was the main physical explanation for observed results.

The analysis of single tracks shows that the large beam – low VED process is more energy efficient (higher penetration dept at the same VED), and generates near elliptical and shallow melt pools, suggesting a conduction welding regime, more stable, instead of usually key-hole welding mode obtained in case of classical *small beam – high VED regime.*

The manufactured 3D parts are almost fully dense for *large beam – low VED condition,* whereas porosities are always present in classical LBM samples. High speed videos exhibit less spatters and almost total absence of vaporization for *large beam – low VED condition,* confirming that the physical origin of porosities is mostly vaporization.

Combining *small beam – high VED* for contours and *large beam – low VED* for hatching areas on each manufactured layer was also shown to allow correct surface roughness with high density. The main drawback of such a modified configuration is the thermal deformations due to higher total energy input through the use of *large beam – low VED*.

A microstructural investigation was also carried out and indicated more elongated columnar grains but the same dislocation density. This was shown to allow similar recrystallization for both *large beam – low VED* and *small beam – high VED* configurations. Moderate improvements of build rates (up to 8 mm^3/s maximum value) were also demonstrated but more optimization of the experimental procedure should allow further enhancement of L-PBF productivity.

Last, a compromise between reduced spatters/increased productivity and increased heat effects will have to be found, maybe by increasing slightly the layer height or increasing the hatch distance.

Author Statement

All authors have seen and approved the final version of the manuscript being submitted.

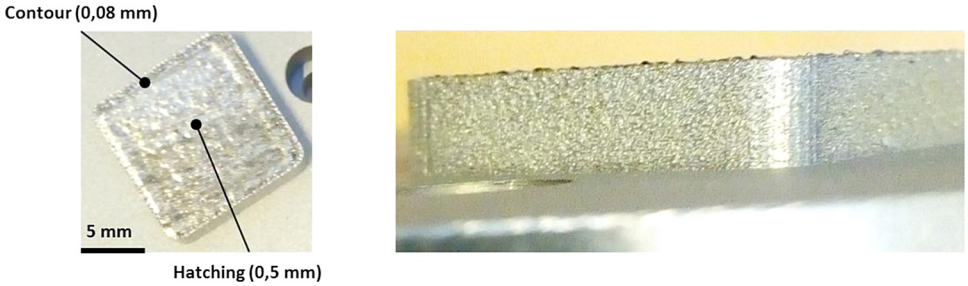

Fig. 14. 3D part obtained by the combination of a small beam – high VED for contour and a large beam – low VED for hatching (P = 1000 W, V = 400 mm/s, hatch = 200 µm).

Declaration of Competing Interest

The authors declare that they have no known competing financial interests or personal relationships that could have appeared to influence the work reported in this paper.

Acknowledgements

This work was carried out within the frame of the FAIR PSPC project granted by BPI France. All the partners of the FAIR project are acknowledged for fruitful discussions.

References

[1] M. Colopi, L. Caprio, A.G. Demir, B. Previtali, Selective Laser melting of pure Cu with a 1 kW single mode fiber laser, Procedia CIRP 74 (2018) 59–63.
[2] M.J. Matthews, G. Guss, S.A. Khairallah, A.M. Rubenchik, P.J. Depond, W.E. King, Denudation of metal powder layers in laser powder bed fusion processes, Acta. Mater. 114 (2016) 33–42.
[3] S.A. Khairallah, A.T. Anderson, A. Rubenchik, W.E. King, Laser-powder bed fusion additive manufacturing: Physics if complex melt flow and formation mechanisms of pores, spatter and denudation zones, Acta Mater. 108 (2016) 36–45.
[4] C. Qiu, C. Panwisawas, M. Ward, H.C. Basoalto, J.W. Brooks, M.M. Attalah, On the role of melt-pool flow into the surface structure and porosity development during selective laser melting, Acta Mater. 96 (2015) 72–79.
[5] M. Ma, Z. Wang, M. Gao, X. Zeng, Layer thickness dependence of performance in high-power selective laser melting of 1Cr18Ni9Ti stainless steel, J. Mater. Process. Technol. 215 (2015) 142–150.
[6] C. Charpentier, P. Lefebvre, F. Briand, F. Edy, S. Abed, P. Peyre, Effect of the gas atmosphere during the Laser Beam Melting Process, Proceedings of Euro PM2018 (Bilbao, Spain) (2018).
[7] W. Meiners, Direktes Selektives Lasersintern einkomponentiger metallischer Werkstoffe, Dissertation, RWTH, Aachen. (1999).
[8] D.B. Hann, J. Iammi, J. Folkes, A simple methodology for predicting laser-weld properties from material and laser parameters, J. Phys. D: Appl. Phys 44 (2011) 445401.
[9] V. Gunenthiram, P. Peyre, M. Schneider, M. Dal, F. Coste, I. Koutiri, R. Fabbro, Experimental analysis of spatter generation and melt-pool behavior during the powder bed laser beam melting process, J. Mater. Process. Technol. 251 (2018) 376–386.
[10] D. Buchbinder, H. Schleifenbaum, S. Heindrich, W. Meiners, J. Bültmann, High power selective laser melting (HP SLM) of Aluminum parts, Physics Procedia 12 (2011) 271–278.
[11] P. Bidare, I. Bitharas, R.M. Ward, M.M. Attalah, A.J. Moore, Laser Powder Bed Fusion in high-pressure atmospheres, The Int. J. of Adv. Manuf. Technol. 99 (2018) 543–555.
[12] H. Schleifenbaum, W. Meiners, K. Wissenback, C. Hinke, Individualized production by mean of high power Selective Laser melting, CIRP J. of Manuf. Sci. and Technol. 2 (2010) 161–169.
[13] T. Heeling, K. Wegener, The effect of multi-beam strategies on selective laser melting of stainless steel 316L, Addit. Manuf. 22 (2018) (2018) 334–342.
[14] M.L. Montero-Sistiaga, M.G. Martinez, K. Boschmans, J.P. Kruth, J.V. Humbeeck, K. Vanmeensel, Microstructure evolution of 316L produced by HP-SLM (high power selective laser melting, Addit. Manuf. 23 (2018) 402–410.
[15] M.L. Montero-Sistiaga, S. Pourbabak, J.V. Humbeeck, D. Schryvers, Martinez, K. Vanmeensel, Microstructure and mechanical properties of Hastelly X produced by HP-SLM (high power selective laser melting), Mater. Des. 165 (2019) 107598.
[16] F. Huber, T. Papke, M. Kerkien, F. Tost, G. Geyer, M. Merklein, M. Schmidt, Z. Florian, Custumized exposure strategies for manufacturing hydrid parts by combining laser beam melting and sheet metal forming, J. Las. Appl. 31 (2019) 022318.
[17] J. Metelkova, Y. Kinds, K. Kempen, C. De Formanoir, A. Witvrouw, B. Van Hooreweder, On the influence of laser defocusing in selective laser melting of 316L, Addit. Manuf. 23 (2018) 161–169.
[18] N.W. Makoana, H. Möller, I. Yadroitsava, I. Yadroitsev, Characterization of 17-4PH Single Tracks Produced at Different Parametric Conditions towards Increased Productivity of LPBF Systems—The Effect of Laser Power and Spot Size Upscaling, Metals 8 (2018) 475, https://doi.org/10.3390/met8070475.
[19] A.M. Rubenchik, W.E. King, S.S. Wu, Scaling laws for additive manufacturing, J. Mater. Process. Technol. 257 (2018) 234–243.
[20] W.E. King, H.D. Barth, V.M. Castillo, G.F. Gallegos, J.W. Gibbs, D.E. Hahn, C. Kamath, A.M. Rubenchik, Observation of keyhole mode laser melting in laser powder bed fusion additive manufacturing, J. Mater. Process. Technol. 214 (2014) 2915–2925.
[21] R. Fabbro, Scaling laws for the laser welding process in keyhole mode, J. Mater. Process. Technol. 264 (2019) 346–351 ff10.1016/j.jmatprotec.2018.09.027.
[22] J. Trapp, A.M. Rubenchik, G. Guss, M. Matthews, In situ absorptivity measurements of metallic powders during laser powder-bed fusion additive manufacturing, Appl. Mat. Today 9 (2017) 341–349.
[23] http://www.specialmetals.com/assets/smc/documents/alloys/inconel/inconel-alloy-625.pdf.
[24] D. Gu, Y. Shen, Balling phenomena in direct laser sintering of stainless steel powder: Metallurgical mechanisms and control methods, Mater. Des. 30 (2009) 2903–2910, https://doi.org/10.1016/j.matdes.2009.01.013.
[25] L.E. Criales, Y.M. Arısoy, B. Lane, S. Moylan, A. Donmez, T. Özel, Laser powder bed fusion of nickel alloy 625: Experimental investigations of effects of process parameters on melt pool size and shape with spatter analysis, Int. J. Mach. Tools. Manuf. 121 (2017) 22–36, https://doi.org/10.1016/j.ijmachtools.2017.03.004.
[26] D.M. Stefanescu, Science and engineering of casting solidification: Third edition, (2015), https://doi.org/10.1007/978-3-319-15693-4.
[27] H. Gao, Y. Huang, W.D. Nix, J.W. Hutchinson, Mechanism-based strain gradient plasticity— I. Theory, J. Mech. Phys. Solids 47 (1999) 1239–1263.
[28] C. Moussa, M. Bernacki, R. Besnard, N. Bozzolo, Statistical analysis of dislocations and dislocation boundaries from EBSD data, Ultramicroscopy. 179 (2017) (2017) 63–72, https://doi.org/10.1016/j.ultramic.2017.04.005.
[29] O.O. Salman, C. Gammer, A.K. Chaubey, J. Eckert, S. Scudino, Effect of heat treatment on microstructure and mechanical properties of 316L steel synthesized by selective laser melting, Mater. Sci. Eng. A 748 (2019) 205–212.
[30] A. Kreitcberg, V. Brailovski, S. Turenne, Effect of heat treatment and hot isostatic pressing on the microstructure and mechanical properties of Inconel 625 alloy processed by laser powder bed fusion, 201, Mater. Sci. Eng. A. 689 (2017) 1–10, https://doi.org/10.1016/j.msea.2017.02.038.